Gravity waves resolved in ECMWF and measured by SABER

S. Schroeder,[1] P. Preusse,[1] M. Ern,[1] and M. Riese[1]

Received 17 December 2008; revised 13 March 2009; accepted 17 April 2009; published 21 May 2009.

[1] The limited resolution of most general circulation models (GCMs) is not sufficient to simulate gravity waves (GWs) explicitly. ECMWF (European Center for Medium-Range Weather Forecasts) data have now a horizontal resolution of $^1/_4°$, so parts of the mesoscale GWs can be resolved although most source processes still contain subgrid phenomena. We validate the GWs resolved in ECMWF by comparison with corresponding results obtained from global SABER (Sounding of the Atmosphere Using Broadband Emission Radiometry) satellite observations. For this comparison, effects of the radiative transfer and satellite retrieval procedure are accounted for. Globally, GWs can be attributed to various GW sources and the GW spectrum is modulated by the background winds. Correlation analysis comparing SABER and ECMWF temperature fluctuations indicate good agreement with respect to mountain waves, for example, over the southern tip of south America or over Scandinavia, as well as GWs at the edge of the winter polar vortex. **Citation:** Schroeder, S., P. Preusse, M. Ern, and M. Riese (2009), Gravity waves resolved in ECMWF and measured by SABER, *Geophys. Res. Lett.*, *36*, L10805, doi:10.1029/2008GL037054.

1. Introduction

[2] Gravity waves (GWs) play a key role in atmospheric dynamics. GWs with tropospheric sources propagate upward and with decreasing air density their amplitudes increase. After reaching the saturation amplitude the waves break, deposit momentum and accelerate or decelerate the background winds. One prominent example is the contribution of breaking GWs to driving the Quasi-Biennial-Oscillation (QBO) [*Dunkerton*, 1997]. Gravity waves are also the main driver of mesospheric winds and the summer time branch of the stratospheric Brewer-Dobson circulation [e.g., *Alexander and Rosenlof*, 2003; *Fritts and Alexander*, 2003].

[3] The resolution of most general circulation models (GCMs) is insufficient for resolving GWs, but in recent years some models were operated at higher resolution so that these models now represent parts of the GW spectrum. Since 1 January 2006 ECMWF data have a horizontal resolution of $^1/_4°$ so that mesoscale waves with wavelength > 150-200 km dependent on latitude can be resolved. Synoptic scale atmospheric features are constantly adjusted by data assimilation, but GWs are almost completely determined by the GCM itself, although GW source processes are still not fully resolved. There are only few case studies comparing GWs resolved in ECMWF directly with measurements [e.g., *Eckermann et al.*, 2006; *Alexander and Teitelbaum*, 2007; *Wu and Eckermann*, 2008]. However, a statistical survey feasible with global, long-term satellite observations, so far is missing. This kind of validation is interesting for a wider community, since many studies use ECMWF wind and temperature data for driving chemical transport and cloud models. Gravity waves are known to induce polar stratospheric clouds, as well as cirrus clouds and are therefore important for heterogeneous chemistry especially for polar ozone depletion and dehydration in the tropical tropopause layer [e.g., *Carslaw et al.*, 1999; *Doernbrack et al.*, 2001; *Jensen et al.*, 2001; *Hoepfner et al.*, 2006]. So far in many studies only the synoptic scales were available from weather service data and mesoscale perturbations had to be inferred from dedicated GW modeling. An accurate representation of GWs provided, future studies could use ECMWF data directly. In this study we compare GWs resolved in operational ECMWF data (T799, N400, 91 hybrid levels) with SABER measurements for the year 2006. A climatology of GW squared amplitudes for altitudes between 20 km and 100 km was derived by *Preusse et al.* [2009]: horizontal wavelengths range from the visibility limit of 100–200 km to global wavenumber 6, vertical wavelengths range from 5 km to 50 km. For an accurate comparison radiative transfer and retrieval effects need to be taken into account. In section 2 we describe the comparison method and show a global survey. In section 3 we discuss GW sources included in both datasets. The results are briefly summarized in section 4.

2. Comparison of Gravity Wave Temperature Amplitudes

[4] Figure 1 shows a typical example of SABER and ECMWF temperature data. Data are taken at 10 August 2006 and 28 km altitude. Temperatures are warmer in the north on the summer hemisphere, colder in the south on the winter hemisphere, and there is a sharp temperature gradient at the edge of the winter polar vortex. Planetary wave 1 and 2 structures are visible in both datasets, most notably at the vortex edge. In this measuring period SABER points southward resulting in a latitudinal coverage from 84°S to 53°N. The viewing direction of the instrument changes every ≈60 days so that the full SABER dataset for 2006 contains measurements between 84°S and 84°N. The SABER viewing geometry is illustrated for a typical satellite orbit shown in Figure 2 for 10 August 2006. SABER views to the right of the orbit with respect to the flight direction. For each altitude profile crosses mark positions of the highest tangent points while the dots mark the according satellite positions. An exemplary line of sight, marked as thick line, is also shown.

[1]Institute of Chemistry and Dynamics of the Geosphere: ICG-1, Research Center Juelich, Juelich, Germany.

0094-8276/09/2008GL037054

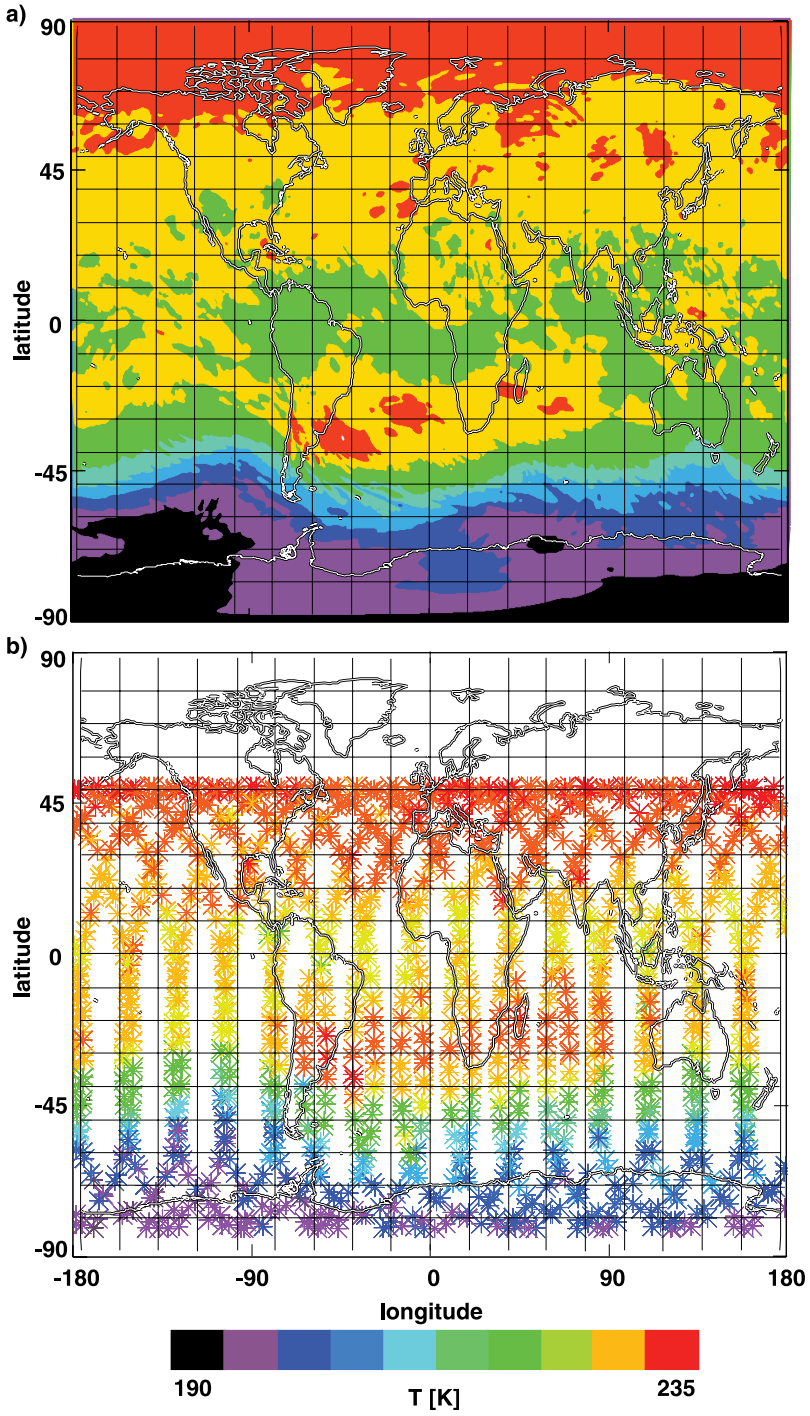

Figure 1. (a) ECMWF and (b) SABER temperature data at 28 km altitude for 10 August 2006; color bar in units of Kelvin.

[5] By using the SABER measurement, the lines of sight (LOS) coordinates are calculated every 0.5 km altitude for all tangent points lower than the maximum ECMWF altitude, i.e. lower than 60 km until January 2006 and 80 km afterwards. Onto these LOS the ECMWF data are interpolated preserving the 0.25° horizontal resolution of the ECMWF data. Effects of the radiative transfer are simulated by convolving the sampled temperatures with a Gaussian weight that has a width of σ = 200 km and peaks at the tangent point [*Preusse et al.*, 2002]. From the resulting data fields temperatures are retrieved using an onion-peeling scheme. In this way we simulate SABER temperature measurements of ECMWF (hereafter refereed to as ECMWF*) data including effects of radiative transfer and retrieval at the SABER measurement locations. Next we isolate the small scale perturbations associated with the GWs from the global scale background temperatures for both data sets. We use a Kalman filter to estimate zonal wavenumbers 0 to 6 for all altitudes and subtract the results from the input data [*Preusse et al.*, 2002]. This approach is applied to both

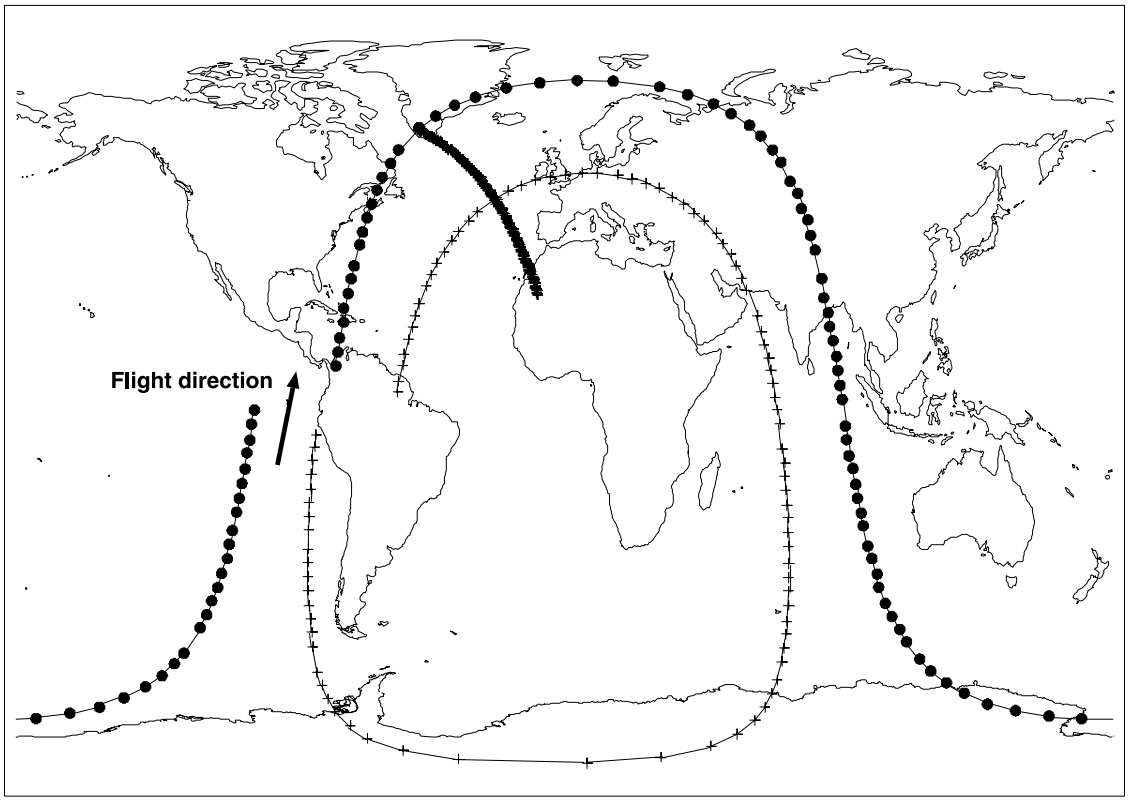

Figure 2. SABER satellite position (line marked with dots) and tangent point position (line marked with crosses) for a single orbit at 28 km tangent height. Also one calculated line of sight is plotted (solid curve) with tangent point over the Atlantic. For details, see text.

SABER measurements and ECMWF* fields. For the regular gridded ECMWF data we can perform a second way of detrending: the ECMWF data are high-pass filtered to contain only zonal wavenumbers larger than 6 by means of a Fourier transformation. Since we use a simplified, linear radiative transfer scheme, the measurement and retrieval simulations can be applied to the temperature perturbations as described above. The wave analysis we use is a combination of maximum entropy method (MEM) and harmonic analysis (HA) to obtain temperature amplitudes of the two dominant wave components, vertical wavelengths and phases for each vertical profile [*Preusse et al.*, 2002]. The resulting squared temperature amplitudes of the wave analysis averaged over 9 to 11 August 2006 are shown in Figure 3. Both data sets are detrended by the Kalman filter and averaged over bins of 20° longitude times 10° latitude.

[6] The horizontal structures in the two maps (SABER (Figure 3a) and ECMWF* (Figure 3b)) are similar. We see higher amplitudes in the south at the edge of the polar vortex and decreasing amplitudes towards the north. Subtropical maxima in the summer hemisphere, presumably due to convection, are in qualitative agreement to the global distributions inferred from AURA-MLS [*Wu and Eckermann*, 2008]. The absolute values deduced from the two instruments cannot be directly compared because of the different observational filters of the two instruments. In particular, SABER covers almost the entire range of waves resolved in ECMWF, whereas MLS resolves primarily waves at shorter horizontal wavelengths and with strongly reduced sensitivity [*Preusse et al.*, 2002, 2008; *Wu and Eckermann*, 2008], resulting in much lower values than for both SABER and ECMWF. However, ECMWF* squared amplitudes are lower by about a factor of two as expressed in the different color bar scaling. The scatterplot in Figure 3c shows the correlation between ECMWF* and SABER squared temperature amplitudes, the black straight line has slope ≈0.58. The calculated correlation coefficient of ≈0.79 confirms the visual conformance of the both maps. In global studies the slope between ECMWF* and SABER temperature amplitudes in our data set has an average value of ≈0.5 below 40 km altitude. Above 40 km damping in the GCM starts and ECMWF* temperature amplitudes decrease. Above 50 km the measured data contain temperature amplitudes with values more than five times higher than in the ECMWF model data.

3. Gravity Wave Source Regions

[7] We next consider the temporal evolution of GW squared amplitudes in Figure 4 for three regions representative of different GW forcing mechanisms. Data are averaged over 2 km altitude and three days and plotted in terms of decibel ($[dB] = [10 \cdot log_{10}(K^2)]$) for better visibility of small temperature amplitudes. At South America, a region dominated by local mountain wave forcing (Figure 4a), SABER and ECMWF* data agree well in their annual cycle as well as in short term variations. The calculated correlation coefficient is 0.90. However, the offset of 3–4 dB indicates that ECMWF* data are lower by a factor of ≈2. In

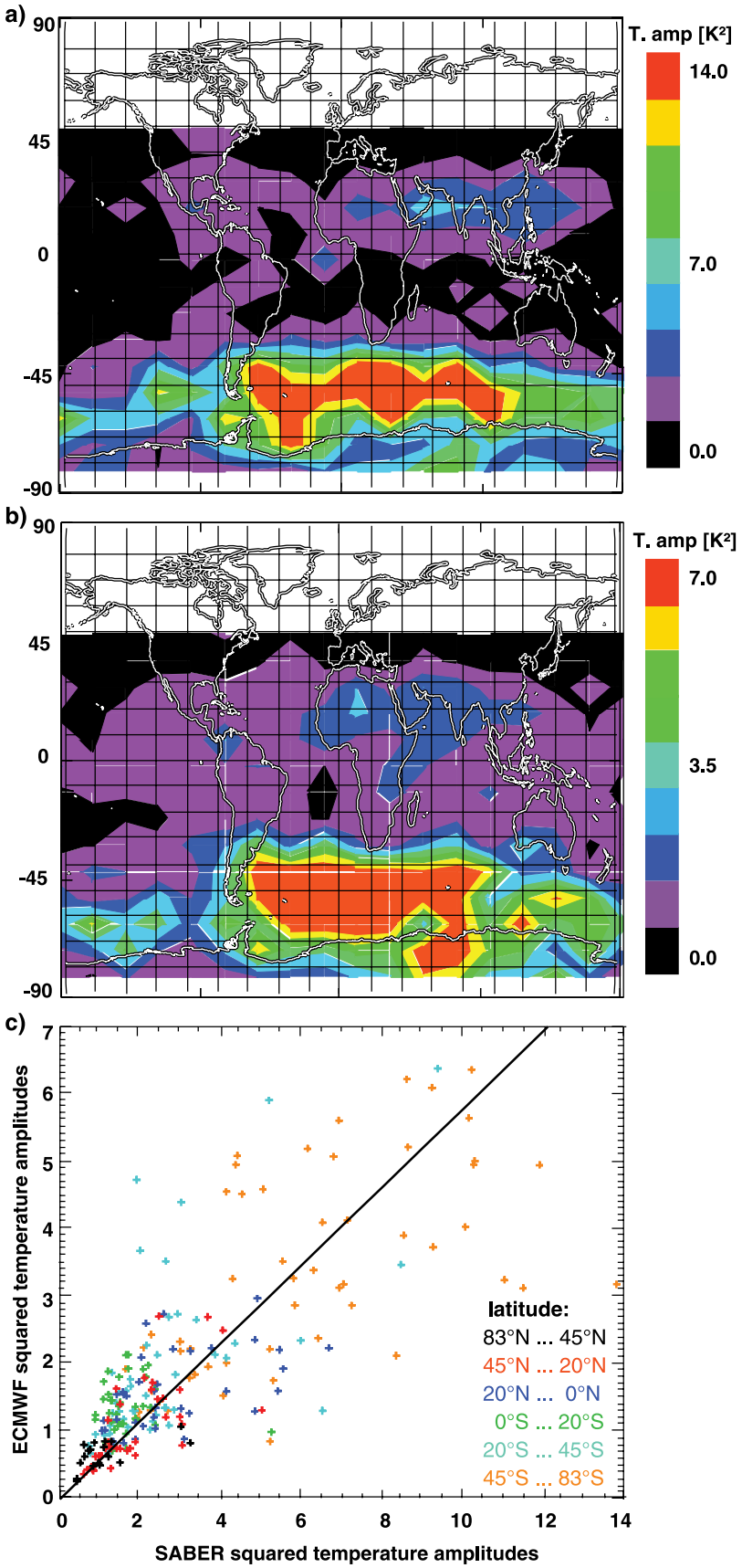

Figure 3. Squared temperature amplitudes [K^2] at 28 km altitude (9–11 August 2006): (a) SABER, (b) ECMWF*, and (c) scatter plot between ECMWF* and SABER. The correlation coefficient is ≈0.79. For details, see text.

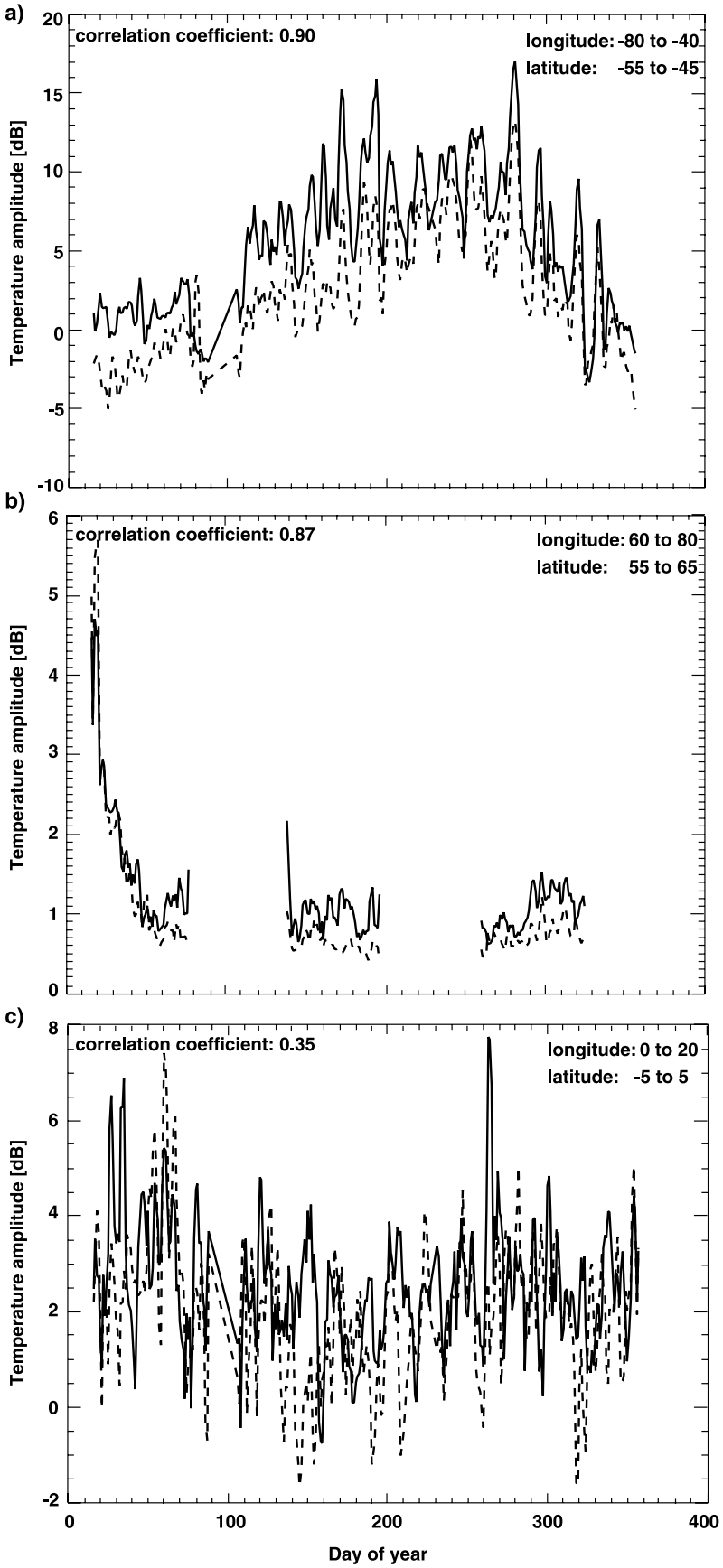

Figure 4. Temperature amplitudes in units of $[dB] = [10 \cdot log_{10}(K^2)]$ at 30 km altitude for different regions: (a) South America, (b) Urals, and (c) Equator. ECMWF*, dashed line; SABER, solid line. For details, see text.

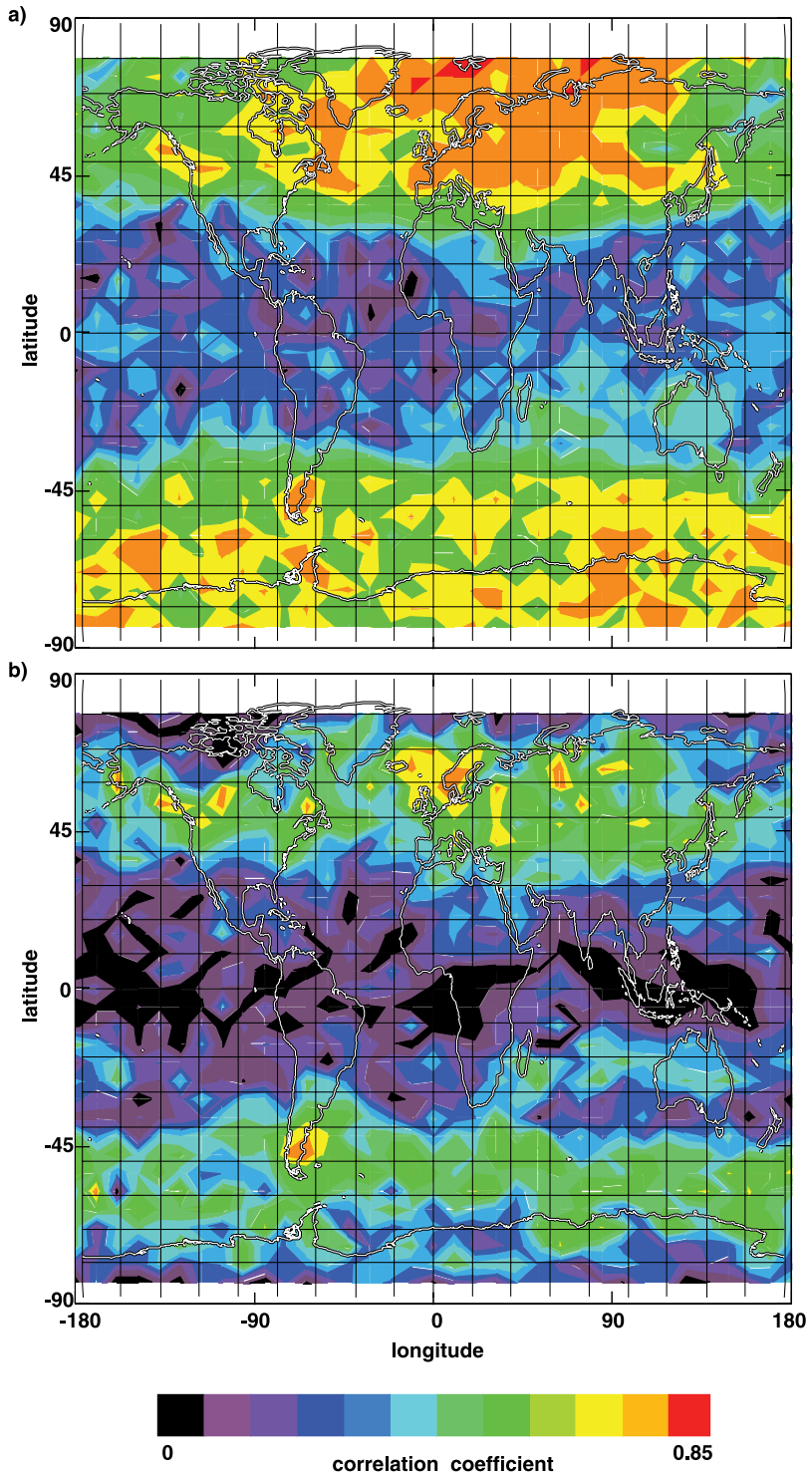

Figure 5. Correlation between ECMWF* and SABER for 2006 at 30 km altitude: (a) ECMWF* and SABER data detrended via Kalman filter and (b) ECMWF* detrended via Fourier transformation and SABER via Kalman filter. For values of the correlation coefficient, see color bar. For details, see text.

Figure 4b another mountain wave region is chosen. In this case the annual and part of the day-to-day variations over the Urals are also well reproduced albeit the squared temperature amplitudes are much lower than over South America. The calculated correlation coefficient is about 0.87. Because the SABER instrument alternates the viewing direction about every 60 days, there are data gaps. For the third region over the equator (Figure 4c) there is only a weak annual variation, which is reproduced. At smaller timescales, however, there is no agreement between both data sets and the resulting correlation coefficient is only 0.35.

[8] We now can use temporal correlations as shown in Figure 4 to identify source regions well represented in

ECMWF. Data are averaged over 10° longitude, 5° latitude, 2km altitude and three days. Correlation coefficients for the resulting time series are calculated. The statistical significance of all correlations shown in this article was tested with a ''random-phase'' test as described by *Ebisuzaki* [1997] and is better than 98%.

[9] Figure 5 shows the correlation coefficients at 30 km altitude. In Figure 5a ECMWF* and SABER data were both detrended via Kalman filter; for Figure 5b ECMWF* data were detrended via Fourier transformation while the SABER data were again detrended via Kalman filter.

[10] In Figure 5a high correlations in the polar and mid latitude regions can be found. The correlations over the mountain wave regions like South America, Scandinavia and the Urals are about 0.8 and are a little lower than in the regions discussed in Figure 4 due to the smaller box size used for the averaging. Also at the coast of Alaska and the northern tip of Antarctica correlations are high. The correlations between Fourier detrended ECMWF* data and Kalman detrended SABER data (Figure 5b) are in general lower than those in Figure 5a, but here the mountain wave dominated regions as, for example, South America, Scandinavia and the Urals are highlighted with high correlations.

[11] While mountain waves and the GW activity in the polar vortices is well represented in the ECMWF* data there are obvious deficients with convectively generated GWs in the tropics. The equatorial region in general shows very low correlations between ECMWF* fields and SABER measurement and also over the Asian monsoon region there are only low correlations.

4. Summary

[12] SABER observations are well suited to validate resolved gravity waves (GWs) in global models such as ECMWF. The comparison between ECMWF temperature fields and SABER satellite measurements shows that ECMWF can well resolve GWs over mountainous regions and at the edge of the Antarctic polar vortex. However, the wave amplitudes are too low by a factor of two. Wave generation by convection is not well represented in the ECMWF model. Above 40 km the altitude, the resolution of ECMWF is reduced and GWs are strongly damped by Rayleigh friction.

[13] **Acknowledgments.** We thank the European Center of Medium-Range Weather Forecasts (ECMWF) for providing the high resolution operational analysis data used in our studies.

References

Alexander, M. J., and K. H. Rosenlof (2003), Gravity-wave forcing in the stratosphere: Observational constraints from the Upper Atmosphere Research Satellite and implications for parameterization in global models, *J. Geophys. Res.*, *108*(D19), 4597, doi:10.1029/2003JD003373.

Alexander, M. J., and H. Teitelbaum (2007), Observation and analysis of a large amplitude mountain wave event over the Antarctic peninsula, *J. Geophys. Res.*, *112*, D21103, doi:10.1029/2006JD008368.

Carslaw, K. S., T. Peter, J. T. Bacmeister, and S. D. Eckermann (1999), Widespread solid particle formation by mountain waves in the Arctic stratosphere, *J. Geophys. Res.*, *104*, 1827–1836.

Doernbrack, A., M. Leutbecher, J. Reichardt, A. Behrendt, K. P. Mueller, and G. Baumgarten (2001), Relevance of mountain wave cooling for the formation of polar stratospheric clouds over Scandinavia: Mesoscale dynamics and observations for January 1997, *J. Geophys. Res.*, *106*, 1569–1581.

Dunkerton, T. J. (1997), The role of gravity waves in the quasi-biennial oscillation, *J. Geophys. Res.*, *102*(D22), 26,053–26,076.

Ebisuzaki, W. (1997), A method to estimate the statistical significance of a correlation when the data are serially correlated, *J. Clim.*, *9*, 2147–2153.

Eckermann, S. D., A. Doernbrack, S. B. Vosper, H. Flentje, M. J. Mahoney, T. P. Bui, and K. S. Carslaw (2006), Mountain wave-induced polar stratospheric cloud forecasts for aircraft science flights during SOLVE/THESEO 2000, *Weather Forecasting*, *21*, 42–68, 2006.

Fritts, D. C., and M. J. Alexander (2003), Gravity wave dynamics and effects in the middle atmosphere, *Rev. Geophys.*, *41*(1), 1003, doi:10.1029/2001RG000106.

Hoepfner, H., et al. (2006), MIPAS detects Antarctic stratospheric belt of NAT PSCs caused by mountain waves, *Atmos. Chem. Phys.*, *6*, 1221–1230.

Jensen, E. J., L. Pfister, A. S. Ackerman, A. Tabazadeh, and O. B. Toon (2001), A conceptual model of the dehydration of air due to freeze-drying by optically thin, laminar cirrus rising slowly across the tropical tropopause, *J. Geophys. Res.*, *106*, 17,237–17,252.

Preusse, P., A. Doernbrack, S. D. Eckermann, M. Riese, B. Schaeler, J. T. Bacmeister, D. Broutman, and K. U. Grossmann (2002), Space-based measurements of stratospheric mountain waves by CRISTA: 1. Sensitivity, analysis method, and a case study, *J. Geophys. Res.*, *107*(D23), 8178, doi:10.1029/2001JD000699.

Preusse, P., S. D. Eckermann, and M. Ern (2008), Transparency of the atmosphere to short horizontal wavelength gravity waves, *J. Geophys. Res.*, *113*, D24104, doi:10.1029/2007JD009682.

Preusse, P., S. D. Eckermann, M. Ern, J. Oberheide, R. Picard, R. Roble, G. Riese, J. Russell III, and M. Mlynczak (2009), Global ray tracing simulations of the SABER gravity wave climatology, *J. Geophys. Res.*, *114*, D08126, doi:10.1029/2008JD011214.

Wu, D. L., and S. D. Eckermann (2008), Global gravity wave variances from Aura MLS: Characteristics and interpretation, *J. Atmos. Sci.*, *65*, 3695–3718, doi:10.1175/2008JAS2489.1.

M. Ern, P. Preusse, M. Riese, and S. Schroeder, Institute of Chemistry and Dynamics of the Geosphere: ICG-1, Research Center Juelich, D-52425 Juelich, Germany. (se.schroeder@fz-juelich.de)